

Sondheimer oscillations as a probe of non-ohmic flow in WP_2 crystals

Maarten R. van Delft ^{1✉}, Yaxian Wang², Carsten Putzke ¹, Jacopo Oswald³, Georgios Varnavides², Christina A. C. Garcia ², Chunyu Guo ¹, Heinz Schmid ³, Vicky Süß⁴, Horst Borrmann ⁴, Jonas Diaz¹, Yan Sun ⁴, Claudia Felser⁴, Bernd Gotsmann ³, Prineha Narang ^{2✉} & Philip J. W. Moll ^{1✉}

As conductors in electronic applications shrink, microscopic conduction processes lead to strong deviations from Ohm's law. Depending on the length scales of momentum conserving (l_{MC}) and relaxing (l_{MR}) electron scattering, and the device size (d), current flows may shift from ohmic to ballistic to hydrodynamic regimes. So far, an in situ methodology to obtain these parameters within a micro/nanodevice is critically lacking. In this context, we exploit Sondheimer oscillations, semi-classical magnetoresistance oscillations due to helical electronic motion, as a method to obtain l_{MR} even when $l_{MR} \gg d$. We extract l_{MR} from the Sondheimer amplitude in WP_2 , at temperatures up to $T \sim 40$ K, a range most relevant for hydrodynamic transport phenomena. Our data on μm -sized devices are in excellent agreement with experimental reports of the bulk l_{MR} and confirm that WP_2 can be microfabricated without degradation. These results conclusively establish Sondheimer oscillations as a quantitative probe of l_{MR} in micro-devices.

¹Laboratory of Quantum Materials (QMAT), Institute of Materials (IMX), École Polytechnique Fédérale de Lausanne (EPFL), Lausanne, Switzerland.

²Harvard John A. Paulson School of Engineering and Applied Sciences, Harvard University, Cambridge, MA, USA. ³IBM Research Europe - Zurich,

Rüschlikon, Switzerland. ⁴Max Planck Institute for Chemical Physics of Solids, Dresden, Germany. ✉email: maarten.vandelft@epfl.ch; prineha@seas.harvard.edu; philip.moll@epfl.ch

In macroscopic metallic wires, the flow of electric current is well described by Ohm's law, which assigns a metal a spatially uniform 'bulk' conductivity. The underlying assumption is that the complex and frequent scattering events of charge carriers occur on the microscopic length scale of a mean free path, which is much smaller than the size of the conductor, d , leading to diffusive behavior. In addition to the scattering processes of bulk systems, the resistance of microscopic conductors is mostly dominated by boundary scattering, thereby masking the internal scattering processes of the bulk in resistance measurements. Here, we present a method to uncover these bulk processes in micro-scale metals, which are of technological importance for fabrication of quantum electronic devices, and simultaneously critical to a fundamental understanding of microscopic current flow patterns. It is instructive to classify the bulk scattering processes into two categories: those that relax the electron momentum, such as electron-phonon, Umklapp or inelastic scattering, occurring at length-scale l_{MR} ; and those that conserve the electron momentum, such as direct or phonon-mediated electron-electron scattering, associated with a length-scale l_{MC} .

Within a kinetic theory framework, these three length scales, namely d , l_{MR} , and l_{MC} , can be used to describe the current flow in micro-scale conductors. When momentum-conserving interactions are negligible, ohmic flow at the macro-scale ($l_{MC} \gg d \gg l_{MR}$) gives way to ballistic transport in clean metals where l_{MR} , $l_{MC} \gg d$. Conversely, when momentum-conserving interactions occur over similar or smaller length scales to momentum-relaxing interactions, a third regime of 'hydrodynamic' transport ($l_{MR} \gg d \gg l_{MC}$) is observable^{1,2}. In this regime, the static transport properties of electron fluids can be described by an effective viscosity that captures the momentum diffusion of the system^{2,3}. These electron fluids exhibit classical fluid phenomena such as Poiseuille flow, whereby the current flow density is greatly decreased at the conductor boundary. Recently, advances in both experimental probes and theoretical descriptions have enabled direct observation of these effects using spatially resolved current density imaging, and have hinted towards the rich landscape of electron hydrodynamics in micro-scale crystals³⁻⁵.

While such local-probe experiments provide means of quantifying electron-electron interactions, and thus extracting l_{MC} , direct measurement of the intrinsic momentum-relaxing processes (l_{MR}) within micron-scale conductors remains elusive, yet is greatly needed. From a practical perspective, l_{MR} describes the overall scattering from impurities and the lattice vibrations within the metallic microstructure, which at low temperature is an important feedback parameter of quality control in fabrication. Furthermore, given both the reduction of sample size and the improved crystal quality, seemingly exotic transport scenarios where $l_{MR} \gg d \gg l_{MC}$ is satisfied are expected to become more prevalent in technology. An accurate description of these length scales is necessary to predict the overall resistance and thus voltage drops and heat dissipation in the nanoelectronic devices. For example, the resistive processes in a hydrodynamic conductor occur at the boundaries rather than homogeneously distributed in the bulk, which alters the spatial distribution of Joule heating and thereby has significant impacts on thermal design.

Real devices will operate at some intermediate state in the d , l_{MR} , and l_{MC} parameter space, departing from the well-understood limiting cases of ohmic, ballistic, and hydrodynamic flow. Rich landscapes of distinct hydrodynamic transport regimes are predicted depending on the relative sizes of the relevant length scales⁶. Effective understanding, modeling and prediction of transport requires an experimental method to estimate these parameters reliably in every regime. In large, ohmic conductors, the bulk mean free path l_{MR} can be simply estimated from the device resistance using a Drude model. Yet when l_{MC} , $l_{MR} \gtrsim d$,

boundary scattering dominates the resistance, and hence estimates of the bulk scattering parameters are highly unreliable. This leaves the worrying possibility of misinterpreting the transport situation in a conductor, in that the microfabrication itself may introduce defects or changes in the bulk properties that remain undetected by macroscopic observables such as the resistance, but have profound impact on the microscopic current distribution. These effects are already noticeable in state-of-the-art transistors, owing to the low carrier density of semi-conductors⁷, but have similarly been reported in metallic conductors⁵. With the increased technological interest in quantum and classical electronics operating at cryogenic temperatures, such questions about unconventional transport regimes are also of practical relevance in next generation electronics⁸.

In this context, we propose to exploit a magneto-oscillatory phenomenon, Sondheimer oscillations (SO), as a self-consistent method to obtain the transport scattering length l_{MR} in-situ, even in constricted channels when $l_{MR} \gg d$. In general, a magnetic field (\mathbf{B}) applied perpendicular to a thin metal forces the carriers on the Fermi surface (FS) to undergo cyclotron motion. Those on extremal orbits of the FS are localized in space due to the absence of a net velocity component parallel to the magnetic field. These localized trajectories can become quantum-coherent, and their interference causes the well-known Shubnikov-de Haas (SdH) oscillations. The states away from extremal orbits also undergo cyclotron motion, yet they move with a net velocity along the magnetic field, analogous to the helical trajectories of free electrons in a magnetic field (Fig. 1). These states are responsible for the Sondheimer size effect which manifests itself as a periodic-in- B oscillation of the transport coefficients, as discovered in the middle of the past century for clean elemental metals⁹.

For any given state, the magnitude of \mathbf{B} sets the helical radius and thus determines how many revolutions the electron completes while traveling from one surface to the other in a micro-device. If an integer number of revolutions occurs, the charge carrier will have performed no net motion along the channel, and hence is semi-classically localized (Fig. 1a). However, if the number of revolutions is non-integer, a net motion along or perpendicular to the channel exists, delocalizing the carriers, resulting in oscillatory longitudinal and transverse magneto-transport behavior. Large-angle bulk scattering events dephase the trajectory, hence the strong sensitivity of SO to the bulk l_{MR} even in nanostructures. These SO are an inherent property of mesoscale confined conductors in three dimensions and have no counterpart in 2D metals like graphene.

The period of the SO is derived by considering a classical charged particle on a helical trajectory between two surfaces perpendicular to the magnetic field¹⁰. One compares the time it takes to travel the distance d between the surfaces, $t_d = d/v_{\parallel}$, to the time to complete a single cyclotron revolution, $\tau_c = 2\pi/\omega_c = 2\pi m^*/eB$ (m^* : effective mass, e : electron charge, $\omega_c = eB/m^*$: cyclotron frequency). Their ratio describes the number of revolutions of the trajectory. For certain fields the helix is commensurate with the finite structure and the number of revolutions is integer, n , such that $t_d = n\tau_c$. This occurs periodically in field, with the period given by:

$$\Delta B = \frac{2\pi m^* v_{\parallel}}{ed} = \frac{\hbar}{ed} \left(\frac{\partial A}{\partial k_{\parallel}} \right). \quad (1)$$

The useful identity $v_{\parallel} = \frac{\hbar}{2\pi m^*} \left(\frac{\partial A}{\partial k_{\parallel}} \right)$, derived by Harrison¹¹, directly relates the SO period to the FS geometry, where v_{\parallel} and k_{\parallel} denote the velocity and momentum component parallel to the magnetic field and A is the FS cross-sectional area encircled by

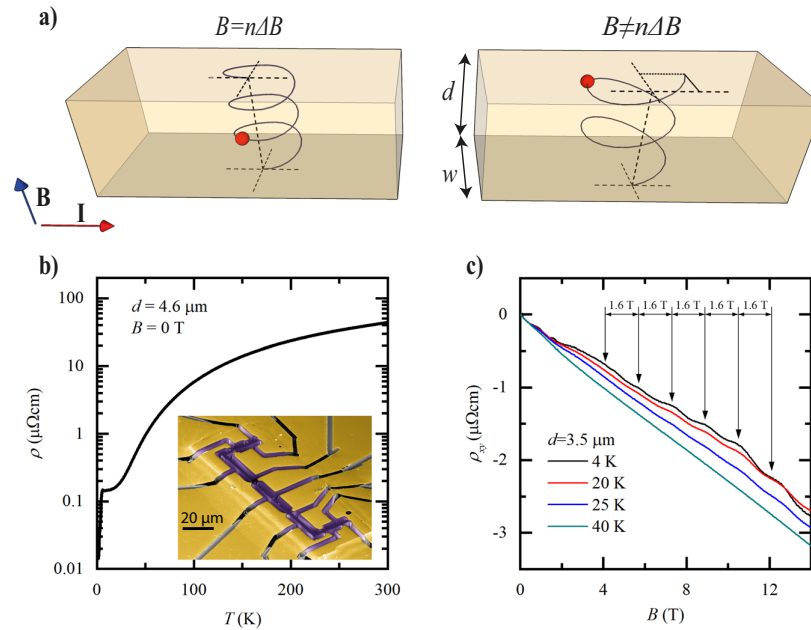


Fig. 1 Introduction to Sondheimer oscillations. **a** Illustration of the Sondheimer effect. Left: the applied magnetic field is $B = 3\Delta B$ and the electron (red) makes an integer number of rotations, with no contribution to transport. Right: $B \neq n\Delta B$. The electron hits the top surface at a different position than its origin on the bottom surface, leading to a contribution to the conductivity. **b** Resistivity as function of temperature for a WP_2 microdevice. Inset: false-color SEM image of a typical device used in this study. **c** Sondheimer oscillations seen in the Hall resistivity of a WP_2 microdevice, for different temperatures. The oscillation period of $\Delta B = 1.6$ T is highlighted.

the orbit in k-space. Note the contrast to conventional QO which appear around extremal orbits, where $\frac{\partial A}{\partial k_{\parallel}} = 0$.

All conduction electrons undergo cyclotron motion, yet depending on $\frac{\partial A}{\partial k_{\parallel}}$, they experience different commensurability fields with a structure of given size d . Hence oscillatory contributions to the total conductivity are washed out, unless a macroscopic number of states share the same $v_{\parallel} \propto \left(\frac{\partial A}{\partial k_{\parallel}}\right)_{E_f}$. In earlier days of Fermiology¹², geometric approximations for FSs, such as elliptical endpoints, were introduced to identify those generalized geometric features that lead to extended regions of constant $\frac{\partial A}{\partial k_{\parallel}}$. The computational methods available nowadays allow a more modern approach to the problem. FSs calculated by ab-initio methods can be numerically sliced in order to calculate their cross-section $A(k_{\parallel})$. We propose to extend this routine procedure, used to find extremal orbits relevant for QO ($\frac{\partial A}{\partial k_{\parallel}} = 0$), to identify SO-active regions ($\frac{\partial^2 A}{\partial k_{\parallel}^2} \sim 0$), based on the Fermi-surface slicing code SKEAF¹³ (see Methods for details on implementation).

SO are caused by the real-space motion of charge carriers and hence also pose some conditions on the shape of the conductor. First, surface scattering needs to be mostly diffusive. If an electron undergoes specular scattering N times before scattering diffusively, it contributes towards the SO as if the sample had an effective thickness Nd ¹⁴, leading to overtones. Naturally, SO vanish in the (unrealistic) limit of perfectly specular boundary conditions, as such ideal kinetic mirrors remove any interaction of the electron system with the finite size of the conductor. Secondly, the conductor must feature two parallel, plane surfaces perpendicular to the magnetic field to select only one spiral trajectory over the entire structure. The parallelicity requirement is simply given by a fraction of the pitch of the spiral at a certain field (maximal thickness variation $\Delta d < v_{\parallel} \tau_c = d \frac{\Delta B}{B}$)¹⁰. These requirements are naturally fulfilled in planar electronic devices.

It is instructive to briefly compare SO to the more widely known QO of resistance, the SdH effect. Both are probes of the FS geometry based on cyclotron orbits, yet the microscopies are strikingly different. While QO frequencies are exclusively determined by FS properties via the Onsager relation and are thus independent of the sample shape, SO are finite-size effects. SO emerge from extended regions on the FS, unlike SdH oscillations to which only states in close vicinity of extremal orbits contribute. While SdH oscillations are quantum interference phenomena, SO are semi-classical, which is key to their use as a robust probe of exotic transport regimes. If both can be observed, powerful statements on the scattering microscopies can be made, as SdH is sensitive to all dephasing collision events and SO separates out the large-angle ones¹⁵. However, the much more stringent conditions of phase coherence in SdH severely limit their observations at higher temperatures. SO are observable up to relatively high temperatures at which the rapidly shrinking $l_{MR}(T)$ leads to a transition into an ohmic state, when $l_{MR}(T) < d$. As such, they are ideally suited to explore the exotic transport regimes in which, for example, hydrodynamic effects occur.

We apply these theoretical considerations to experimentally investigate the scattering mechanisms in micron-sized crystalline bars of the type-II Weyl semimetal WP_2 ¹⁶ exploiting the Sondheimer effect. Bulk single crystals of WP_2 are known for their long l_{MR} , in the range of 100–500 μm ^{17–19}, comparable to the elemental metals in which SO were initially discovered^{20–23}. These are an ideal test case for non-ohmic electron flow, as hydrodynamic transport signatures and nontrivial electron-phonon dynamics have been observed in various topological semimetals^{17,18,24–26}. These ultra-pure crystals are then reduced in size by nanofabrication techniques into constricted channels, to study hydrodynamic or ballistic corrections to the current flow.

Here we employ Focused Ion Beam (FIB) micromachining²⁷, which allows precise control over the channel geometry in 3D. In

this technique, we accelerate Xe ions at 30 kV to locally sputter the target crystal grown by chemical vapor transport (CVT)^{19,28} until a slab of desired dimensions in the μm -range remains. This technique leads to an amorphized surface of around 10 nm thickness, yet has been shown to leave bulk crystal structures pristine²⁹. Naturally, reducing the size of a conductor even without altering its bulk mean free path significantly changes the device resistance at low temperatures due to finite size corrections³⁰. Hence, measurements of the constricted device resistance alone cannot exclude the possibility of bulk degradation due to the fabrication. Thus far, one could only argue based on size-dependent resistance studies that the values smoothly extrapolate to the bulk resistivity value in the limit of infinite device size^{18,31}. Measuring SO directly in the microfabricated devices themselves, however, quantitatively supports that the ultra-high purity of the parent crystal remains unchanged by our fabrication. We note that the fundamental question of the bulk parameters is universal in mesoscopic conducting structures irrespective of the fabrication technique, and these considerations are thus equally applicable to structures obtained by mechanically or chemically thinned samples as well as epitaxially grown crystalline films. SO should provide general insights into the material quality in the strongly confined regime, allowing to contrast different fabrication techniques.

Results

We measure our μm -confined devices using standard lock-in techniques with applied currents between 50 and 100 μA , low enough to limit self-heating, and magnetic fields up to 18 T. At high temperatures, the measured resistivity agrees well with previous reports on high quality bulk crystals, as expected given the momentum-relaxing limited mean free path of charge carriers in this regime (Fig. 1b). Yet in the low temperature limit, the device resistance exceeds that of bulk crystals by more than an order of magnitude^{17,19,32}. Conversely, the residual resistance ratios in our devices ($\text{RRR} \approx 160\text{--}300$) are also considerably lower than in bulk crystals³². The main question we address by SO is whether this excess resistance points to fabrication-induced damage, finite size corrections, or a mixture thereof. At low temperatures around 3 K, a drop in resistance signals a superconducting transition. As WP_2 in bulk form is not superconducting, this likely arises from an amorphous W-rich surface layer due to the FIB fabrication similar to observations made in NbAs ³³ and TaP ³⁴. In Fig. 1c, we show the Hall resistivity, ρ_{xy} , of one of our devices as a function of the magnetic field, for different temperatures. The Hall signal comprises oscillations with a period of $\Delta B = 1.6$ T, resolved above approximately $B = 2$ T.

The staircase device. A hallmark signature of SO is their linear frequency dependence on the device thickness perpendicular to the field. For this reason, we fabricated crystalline devices with multiple sections of different thickness to study the dependence on the channel thickness, d , in a consistent manner. This ‘staircase’ device allows the simultaneous measurement of transport on 5 steps, as illustrated in Fig. 2. SO appear in all transport coefficients, magnetoresistance (MR) and Hall effect alike, yet here we focus on the Hall effect for two practical reasons. First, the step edges induce non-uniform current flows, and hence the device would need to be considerably longer to avoid spurious voltage contributions from currents flowing perpendicular to the device in a longitudinal resistance measurement. Second, WP_2 exhibits a very large MR yet a small Hall coefficient, as typical for compensated semi-metals. Therefore, the SO are more clearly distinguishable against the background in a Hall measurement, but they are also present in the longitudinal channel.

The fabrication process of our WP_2 devices follows largely the same procedure as described in ref. ²⁷. However, for the staircase device, a few key changes were made. In the first fabrication step, the FIB is used to cut a lamella from a bulk WP_2 crystal. One side is polished flat, and the other side polished into five sections, each to a different thickness (Fig. 2b). It is then transferred, flat side down, into a drop of araldite epoxy on a sapphire substrate and electrically contacted by Au sputtering (Fig. 2b). In a second FIB step, the staircase slab is patterned laterally into its final structure (Fig. 2a). We use Xe ions for the entire FIB fabrication process in order to avoid potential issues with Ga ion implantation leading to changes in the carrier density. Indeed, experimentally, we see no indication of any charge carrier modulation.

All segments of the staircase devices show pronounced B -periodic oscillations in the Hall channel, from which the linear background is removed by taking second derivatives. (Fig. 3). At the lowest fields, a weak, aperiodic structure is observed. In this regime, the cyclotron diameter does not fit into the bar, preventing the formation of the Sondheimer spirals. Note that in all devices of different thickness, this onset field of the SO is the same. This is a natural consequence of the fact that the lateral size, perpendicular to the magnetic field, by design, is the same for all steps of the staircase. Each step, however, differs in thickness d parallel to the magnetic field, and the period varies accordingly between steps (Fig. 3b). At even higher fields, the onset of regular SdH oscillations hallmarks a transition into a different quantized regime. The SO frequency $F = 1/\Delta B$ varies linearly with d as expected (Fig. 3c, Eq. (1)).

Sondheimer oscillations. Next we identify the Sondheimer-active region on the FS from the ab-initio band structure, which was calculated by density functional theory (DFT) with the projected augmented wave method as implemented in the code of the Vienna ab-initio Simulation Package³⁵. The FS of WP_2 consists of two types of spin-split pockets: dogbone-shaped electron pockets and extended cylindrical hole pockets (see Fig. 4 and Supplementary Fig. 2 for a complete picture of the FS).

Only one area quantitatively agrees with the observed SO periodicity: the four equivalent endpoints of the dogbone (colored orange in Fig. 3f). Slicing all Fermi-surfaces using SKEAF¹³, their cross-sections $A(k_{\parallel})$ are obtained. While in QO analysis this information is discarded once the extremal orbits are identified, it forms the basis of the SO analysis. As the dogbone is sliced from the endpoints, the area continuously grows until the two endpoint orbits merge and the area abruptly doubles. Slicing further, the area grows until the maximum orbit along the diagonal is reached. The mirror symmetry of the FS enforces then a symmetric spectrum when slicing further beyond the maximum. The quasi-linear growth at the endpoints signals an extended area of Sondheimer-active orbits. Averaging the near-constant derivative in this region, $\frac{\partial A}{\partial k_{\parallel}}$, provides via Eq. (1) a tuning-parameter-free prediction of the thickness dependence of the SO frequency. This ab-initio prediction (red line in Fig. 3c) is in excellent agreement with the observed thickness dependence.

Next the temperature-dependence of the SO amplitude is used to gain direct information about the microscopic scattering processes acting on this region of the FS. In Fig. 4a, b, we plot this temperature dependence and highlight two regimes: that of quantum coherence and that of purely SO. In the first regime, quantum coherence leads to SdH oscillations; however, for typical effective masses $m^* \approx m_e$, as in WP_2 , they are only observable at very low temperatures ($T < 5$ K). Importantly, their quick demise upon increasing temperature is not driven by the temperature dependence of the scattering time, but rather by the broadening of the Fermi-Dirac distribution. This is apparent as their temperature

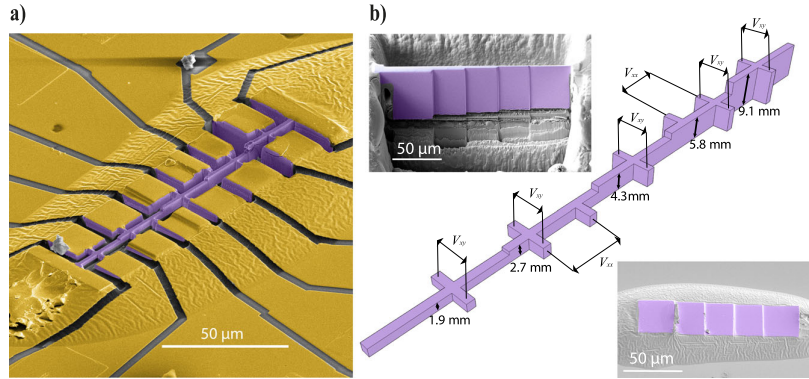


Fig. 2 The staircase device. **a** False color SEM image of a staircase device, used to measure Sondheimer oscillations for different thicknesses. The crystal is colored in purple, and gold contacts in yellow. **b** Main: Schematic of the staircase device, illustrating all possible measurement configurations as well as the thickness of each section. Top left: SEM image of the lamella that will become the device shown in **a**, prior to extracting it from its parent crystal. Bottom right: SEM image of the same lamella, glued down onto a sapphire substrate, ready to define the device geometry. The lamella and glue are covered in gold (not colored) throughout the full field of view. The magnetic field is applied perpendicular to the structure, aligned along the crystallographic [011] direction.

dependence is well described by the Lifshitz–Kosevich formalism based on a temperature-independent quantum lifetime, τ_q .

This strong temperature-suppression of QO severely limits their use to probe scattering mechanisms at elevated temperatures. SO, on the other hand, do not rely on quantum coherence and are readily observed to much higher temperatures, up to 40 K in WP₂, while their temperature decay allows a direct determination of the transport lifetime, $\tau_{MR} = l_{MR}/v_F$. Hence SO make an excellent tool to study materials in the temperature range pertinent to exotic transport regimes like ballistic or hydrodynamic. They self-evidence non-diffusive transport as they only vanish when $l_{MR} \sim d$, and hence are only absent in situations of conventional transport within a given device.

Discussion

Key to observable SO is that electrons do not undergo large-angle scattering events on their path between the surfaces. We therefore have the condition that $l_{MR} > d$ ^{36,37}. As $l_{MR}(T)$ decreases with increasing temperature and the boundary scattering is assumed to be temperature-independent, the SO amplitude is suppressed as $e^{-d/l_{MR}(T)}$ which allows us to estimate the bulk transport mean free path within a finite-size sample, even when $d \ll l_{MR}$. It is extracted as³⁶:

$$\frac{1}{l_{MR}(T)} = -\frac{1}{d} \ln \frac{A(T)}{A(0)}, \tag{2}$$

where $A(T)$ is the SO amplitude at temperature T . $A(T=0)$ is estimated by extrapolation, which is a robust procedure as the SO amplitude saturates at low but finite temperatures. This is analogous to the saturation of the resistivity of bulk metals at low temperatures, once bosonic scattering channels are frozen out and temperature-independent elastic defect scattering becomes dominant.

In the following discussion, we focus on the scattering time τ_{MR} to facilitate comparison of our results with literature and theory, using the average Fermi velocity on the dogbone FS determined from our band structure calculations self-consistently, $v_F = 3.6 \times 10^5$ m/s. The $\tau_{MR}(T)$ obtained from all devices quantitatively agrees, despite their strong difference in thickness (between 1.3 and 4.6 μm) and hence SO frequency, further supporting the validity of this simple analysis (see Fig. 4c and Supplementary Fig. 5). The lifetimes on the SO devices furthermore agree with measurements on bulk crystals¹⁸, evidencing that the increased

resistivity compared to bulk can be wholly attributed to finite size corrections rather than to any fabrication-induced damage, and that FIB fabrication does not introduce significant changes to the bulk properties of WP₂ that might cause misinterpretations of the scattering regime.

For our WP₂ devices, a standard Dingle analysis¹⁵ of the QO yields a quantum scattering time $\tau_q \sim 10^{-13} - 10^{-12}$ s (Fig. 4c), in agreement with published values for bulk crystals WP₂¹⁹. As τ_q is sensitive to all dephasing scattering events, but τ_{MR} only to large-angle momentum-relaxing scattering, the microscopics of the scattering processes in WP₂ are brought to light. The four orders of magnitude difference between τ_{MR} and τ_q reflects a common observation in topological semi-metals such as Cd₃As₂³⁸, PtBi₂³⁹, or TaAs⁴⁰.

Long τ_{MR} , together with a high quality, clean sample, enables the realization of the hydrodynamic regime where the momentum-conserving scattering dominates. These quantitative measurements of τ_q and $\tau_{MR}(T)$ can now be directly compared to theoretical models of scattering. We consider an initial electronic state with energy $\epsilon_{n\mathbf{k}}$ (where n and \mathbf{k} are the band index and wavevector respectively) scattering against a phonon with energy $\omega_{\mathbf{q}\nu}$ (where ν and \mathbf{q} are the phonon polarization and wavevector respectively), into a final electronic state with energy $\epsilon_{m\mathbf{k}+\mathbf{q}}$. The electron–phonon scattering time $\tau_{e\text{-ph}}$ describing such an interaction can be obtained from the electron self energy using Fermi’s golden rule:

$$\tau_{e\text{-ph}}^{-1}(n\mathbf{k}) = \frac{2\pi}{\hbar} \sum_{m\nu} \int_{\text{BZ}} \frac{d\mathbf{q}}{\Omega_{\text{BZ}}} |g_{mn,\nu}(\mathbf{k}, \mathbf{q})|^2 \times \left(n_{\mathbf{q}\nu} + \frac{1}{2} \mp \frac{1}{2} \right) \delta(\epsilon_{n\mathbf{k}} \mp \omega_{\mathbf{q}\nu} - \epsilon_{m\mathbf{k}+\mathbf{q}}), \tag{3}$$

where Ω_{BZ} is the Brillouin zone volume, $f_{n\mathbf{k}}$ and $n_{\mathbf{q}\nu}$ are the Fermi–Dirac and Bose–Einstein distribution functions, respectively, and the electron–phonon matrix element for a scattering vertex is given by

$$g_{mn,\nu}(\mathbf{k}, \mathbf{q}) = \left(\frac{\hbar}{2m_0\omega_{\mathbf{q}\nu}} \right)^{1/2} \langle \psi_{m\mathbf{k}+\mathbf{q}} | \partial_{\mathbf{q}\nu} V | \psi_{n\mathbf{k}} \rangle. \tag{4}$$

Here $\langle \psi_{m\mathbf{k}+\mathbf{q}} |$ and $|\psi_{n\mathbf{k}} \rangle$ are Bloch eigenstates and $\partial_{\mathbf{q}\nu} V$ is the perturbation of the self-consistent potential with respect to ion displacement associated with a phonon branch with frequency

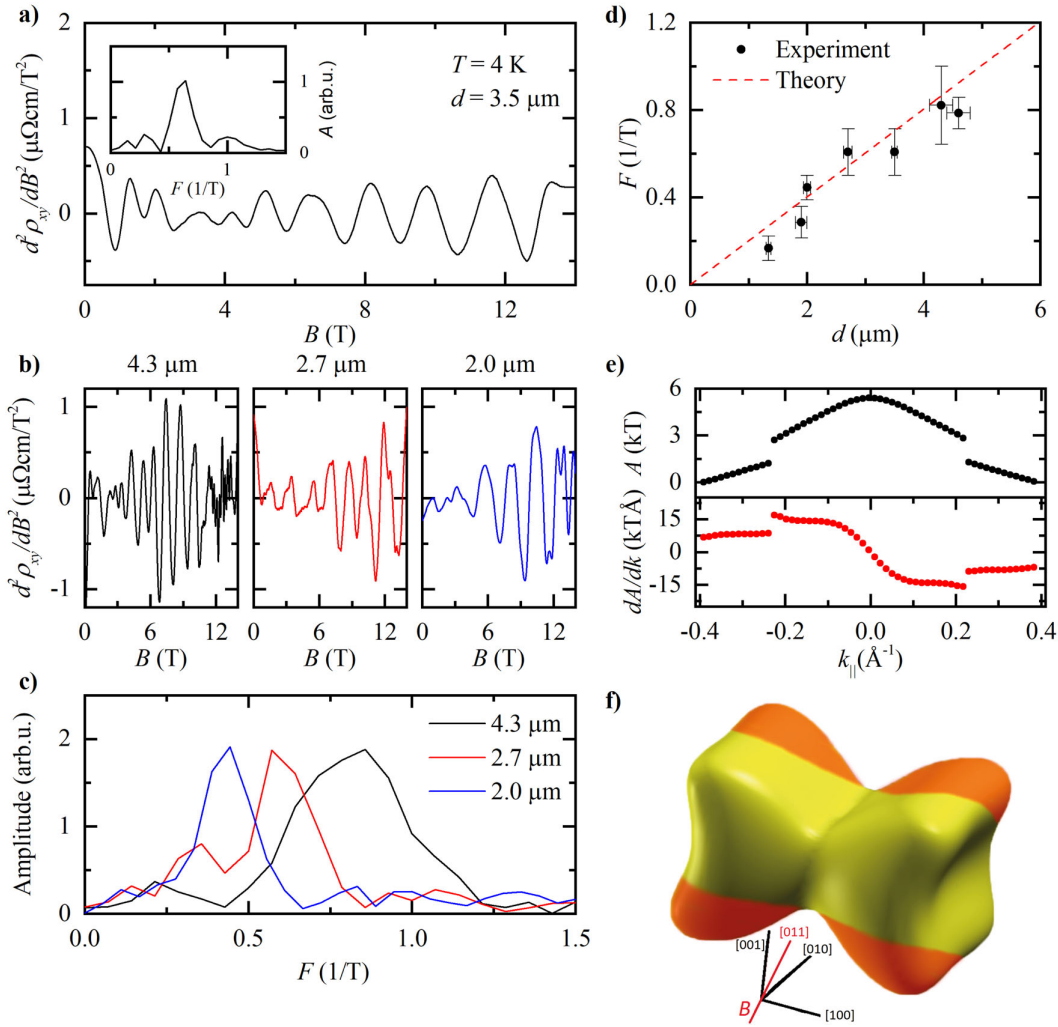


Fig. 3 Analysis of Sondheimer oscillations in WP₂. **a** Second derivative of the Hall resistivity shown in Fig. 1c at $T = 4$ K. Inset: Fast Fourier Spectrum (FFT) corresponding to this data. **b** Second derivatives of the Hall resistivity at three different thicknesses, $d = 4.3, 2.7$ and 2.0 μm , $T = 4$ K. **c** FFTs corresponding to the data in **b**. **d** Dependence of the Sondheimer frequency on d . The error bars in the frequency, F , are derived from the width of the relevant peaks in the FFT spectra and those in d from the standard deviation of thickness measurements made with SEM. The red dashed line is calculated from the Fermi surface as determined from DFT. **e** Cross-sectional area, A , of the dogbone Fermi surface pocket of WP₂ as a function of k parallel to the field direction of our experiments (top), and its derivative (bottom). **f** Location of observed Sondheimer orbits drawn in orange on the dogbone-shaped Fermi surface pocket. The magnetic field is applied along the [011]-direction, perpendicular to the current, as indicated by the red line.

$\omega_{\mathbf{q}\nu}$. Plotting these state-resolved electron–phonon lifetimes at ~ 10 K on the FS reveals the distribution of scattering in the SO-active regions (Fig. 4d). Equation (3), however, accounts, to first order, for all electron–phonon interactions, irrespective of the momentum transfer or equivalently the scattering angle. To remedy this, we augment the scattering rate with an ‘efficiency’ factor⁴¹ given by the relative change of the initial and final state momentum ($1 - \frac{v_{\mathbf{n}\mathbf{k}} \cdot v_{\mathbf{n}\mathbf{k}}}{|v_{\mathbf{n}\mathbf{k}}||v_{\mathbf{n}\mathbf{k}}|} = 1 - \cos \theta$), where $v_{\mathbf{n}\mathbf{k}}$ is the group velocity and θ is the scattering angle:

$$\begin{aligned} \left(\tau_{e-\text{ph}}^{\text{mr}}(\mathbf{n}\mathbf{k})\right)^{-1} &= \frac{2\pi}{\hbar} \sum_{m\nu} \int_{\text{BZ}} \frac{d\mathbf{q}}{\Omega_{\text{BZ}}} |g_{m\nu}(\mathbf{k}, \mathbf{q})|^2 \\ &\times \left(n_{\mathbf{q}\nu} + \frac{1}{2} \mp \frac{1}{2} \right) \delta(\varepsilon_{\mathbf{n}\mathbf{k}} \mp \omega_{\mathbf{q}\nu} - \varepsilon_{\mathbf{m}\mathbf{k}+\mathbf{q}}) \quad (5) \\ &\times \left(1 - \frac{v_{\mathbf{n}\mathbf{k}} \cdot v_{\mathbf{n}\mathbf{k}}}{|v_{\mathbf{n}\mathbf{k}}||v_{\mathbf{n}\mathbf{k}}|} \right). \end{aligned}$$

At low temperatures, the thermally activated phonon modes have a tiny \mathbf{q} , therefore the initial and final electronic states only differ from a small angle. It is thus important to take this momentum-relaxation efficiency factor into account in addition to $\tau_{e-\text{ph}}$ in order to estimate τ_{MR} which determines the electron mean free path in the SO-active regions. In the SO measurements, the electron orbits are located on the endpoints of the dogbone-shaped electron pockets (Fig. 3f), therefore we highlight the scattering efficiency distribution on the electron FS in Fig. 4e. Indeed, when the orbit is aligned along the diagonal direction, the FS cross section features very low scattering efficiency with an averaged $1 - \cos \theta < 0.1$. This supports our observation of frequently scattering electrons with long transport lifetimes in the SO measurement.

These results demonstrate the power of the Sondheimer size effect for the extraction of the momentum-relaxing mean free path in mesoscopic devices when $d \ll l_{\text{MR}}$ via their temperature

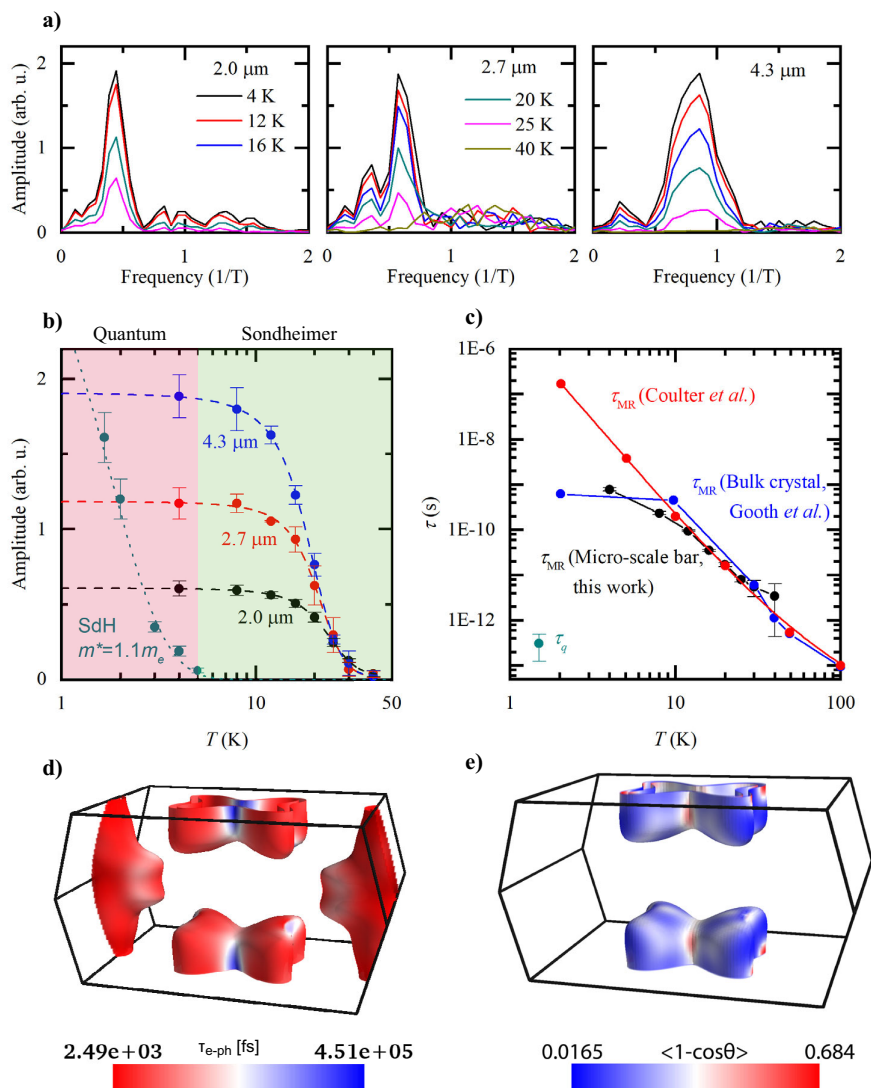


Fig. 4 Extraction of scattering times from the Sondheimer amplitude. **a** FFTs of the SO at different temperatures for thicknesses of 4.3, 2.7, and 2.0 μm . The data at $T = 4\text{ K}$ is the same as that in Fig. 3c. **b** Temperature dependence of the Sondheimer and SdH oscillation amplitudes, for different sample thicknesses. The error bars are estimated from the variation in amplitude in the FFT spectra. The dashed lines are fits used to extrapolate to the amplitude at zero temperature, $A(0)$ (see Methods for details). The dotted line is a Lifshitz-Kosevich fit, giving an effective mass of $1.1m_e$. Two regimes are highlighted: that of quantum coherence, where SdH oscillations exist alongside SO, and that of Sondheimer, where only SO exist. **c** Scattering times extracted for a 4.3 μm thick section of a WP_2 device using Eq. (2) and the calculated Fermi velocity, $v_F = 3.6 \times 10^5\text{ m/s}$. An approximate quantum lifetime extracted from the SdH oscillations as well as data from refs. ^{18,46} are included for comparison. Errors in τ_{MR} are propagated from those in the amplitudes and the error in τ_q is the standard deviation of several measurement. **d** Calculated scattering time for all electron-phonon scattering (τ_{e-ph}) and **e** the scattering efficiency determining the momentum-relaxing scattering lifetimes (τ_{MR}) projected onto the Fermi surface at $T = 10\text{ K}$.

dependence. Combined with first-principles theoretical calculations, we were able to locate the states contributing to the helical motion to the elliptical endpoints of a particular FS of WP_2 . We note, however, that such analysis as well as the thickness dependence are only relevant for the academic purpose of robustly identifying these oscillations as SO. Once this is established, the relevant lifetimes may straightforwardly be obtained from the resistance oscillations at a single thickness. Hence, SO promise to be a powerful probe to obtain the bulk mean free path in devices with μm -scale dimensions without relying on any microscopic model assumptions. This analysis is a clear pathway to identify scattering processes in clean conductors within operating devices. It thereby provides important feedback of the materials quality

after a micro-/nano-fabrication procedure and disentangles the roles of bulk and surface scattering that are inseparably intertwined in averaged transport quantities of strongly confined conductors, such as the resistance. As their origin is entirely semiclassical, they are not restricted by stringent criteria such as quantum coherence and thus span materials parameters of increased scattering rate. In particular, they survive up to significantly higher temperatures and thereby allow microscopic spectroscopy in new regimes of matter dominated by strong quasiparticle interactions, such as hydrodynamic electron transport. With this quantitative probe, it will be exciting to test recent proposals of exotic transport regimes and create devices that leverage such unconventional transport in quantum materials.

Methods

Crystal growth. High quality crystals of WP_2 were grown via the CVD method using iodine as transport agent, with the following starting materials: red phosphorus (Alfa-Aesar, 99.999%) and tungsten trioxide (Alfa-Aesar, 99.998%). The starting materials were sealed in an evacuated fused silica ampoule. A two-zone-furnace with a temperature gradient of 1000–900 °C was used for the CVD method. After several weeks, the ampoule was removed from the furnace and quenched in water. The crystals were characterized by X-ray diffraction.

Fabrication of the staircase device. In Fig. 2, we have shown the so-called staircase device which was especially designed for the measurement of SO. Here, we describe its fabrication in detail, beginning from a bulk crystal. Firstly, the crystallographic orientation of the bulk crystal is determined through XRD measurements, and it is glued in the desired orientation onto an SEM stub. It is then introduced into a Helios G4 PFIB UxX DualBeam FIB/SEM using Xe ions, hence avoiding issues associated with surface implantation as in the more common Ga-based sources. The focused beam of Xe ions is used to cut a rectangular slab we call a lamella from that crystal in three steps. The first is using a high 2.5 μA current to cut two gaps into the crystal, separated by an $\sim 15 \mu\text{m}$ thick and $150 \mu\text{m}$ long section of crystal. A smaller current of $0.2 \mu\text{A}$ is then used to smoothen this crystal section in order to produce moderately flat sidewalls, after which the wall is cut near the bottom and on the sides such that we have a lamella attached to the parent crystal through two beams at its top.

At this stage, a 15 nA current is used to fine-cut both sides of the lamella, leaving it with parallel sidewalls and a high level of smoothness. The thickness of the lamella is now that of what will be thickest section of the staircase device. The lamella is then divided into five sections; the three middle sections are of equal length, while the sections on either end are longer for further contacts. Starting from one side, we leave the first section untouched and polish and mill the other sections to their respective target thickness using cleaning-cross-sections as the milling strategy. This is the stage shown in the top left insert of Fig. 2b. After this, we cut through the beam on one side and thin down the other side.

An ex-situ micromanipulator is used to break the thinned beam and pick up the stepped lamella. On a sapphire substrate with lithographically prepatterned gold contact pads, we place a small droplet of Araldite epoxy. While the epoxy is still liquid, we place our lamella, flat side down, onto the droplet. Capillary forces then create a profile of epoxy around the lamella that extends smoothly up to each of its top surfaces, without covering any. After curing the epoxy for 1 h at 150 °C, we take the substrate to a sputtering machine, where it is briefly RF etched and 3 nm of Ti plus 200 nm of Au are sputtered onto the lamella, glue and prepatterned gold contacts through a shadow mask. The lamella after this step is shown in the bottom right of Fig. 2b.

In order to pattern the device, we again make use of the Helios G4 PFIB. The Ti/Au layer that covers what will be the active part of the device is first removed with an acceleration voltage of 5 kV and an ion current of 2 nA. The overall shape of the device with the position of the contacts is then cut out at 0.3 nA and 30 kV and the central bar of the device is gently polished in order to create smooth sidewalls. Finally, the Ti/Au layer away from the device is cut through in order to separate the contact pads and make sure that current can only flow through the device, which is then ready for measurement.

In order to check that the crystallographic orientation of the final device is as expected based on the initial XRD measurements, we perform measurements of the MR. The MR has a characteristic shape with a minimum for $\mathbf{B} \parallel \mathbf{c}$ and a maximum for $\mathbf{B} \parallel \mathbf{b}$ ¹⁹, allowing an identification of these axes. In Supplementary Fig. 1, we show an angle-dependent measurement of MR for one of our devices, which is indeed aligned 45° away from the *b* and *c* axes.

Calculation of $A(k)$ and $\frac{dA}{dk}$. The calculations of the *k*-dependent cross-sectional area of the FS shown in Fig. 3 and Supplementary Fig. 3 were performed with a slightly modified version of SKEAF¹³, a commonly used software designed to numerically extract QO frequencies from calculated band structures. QO take place at extremal areas of the FS (i.e. when $\frac{dA}{dk} = 0$) and their frequency relates to the extremal area as given by the Onsager relation¹⁵: $F = \frac{h}{2\pi e} A$. This correspondence allows us to display $A(k)$ in units of kT rather than $1/\text{\AA}^2$. As QO are more known than SO, this choice of unit facilitates their comparison.

The SKEAF algorithm, written in the Fortran 90 language, reads electronic structures calculated by DFT in the Band-XCrySDen-Structure-File format. It constructs a cubic super cell much larger than the original reciprocal unit cell and aligned with the magnetic field direction. This super cell is then divided into slices perpendicular to the magnetic field, and the software records the cross-sectional area for each slice. During regular use, SKEAF then matches the orbits over the different slices and finds the extremal ones. We, however, need the area for each slice, and hence we have added a short section of code to create a new file containing the *k*-values and areas (in both $1/\text{\AA}^2$ and kT) for all orbits.

This file contains many copies of each FS sheet. Rather than averaging each orbit, as is done by SKEAF for the extremal orbits, we simply select one copy and plot this as in Fig. 3e. This is reasonable, as the differences between the areas of the copies are consistently less than 0.1%. Finally, we take a numerical derivative of $A(k)$ and find $\frac{dA}{dk}$, from which we can identify possible Sondheimer orbits.

Extraction of I_{MR} from the SO amplitude. We follow a step-by-step procedure in order to extract the I_{MR} as a function of temperature. In the first step, the measured longitudinal or Hall resistivity is smoothed and differentiated twice. The required level of smoothing is adjusted for each dataset to the extent that no oscillatory component of the data is removed, while the noise is suppressed. Importantly, the same procedure is performed consistently for each temperature. After taking the second derivative, we perform an FFT of the data using a Hanning window. The relevant amplitude $A(T)$ is found from the peak in the FFT and plotted against the temperature (see Fig. 4b). In order to extract $A(0)$, we then need to extrapolate to $T = 0 \text{ K}$. In order to do this, we use a fit of the form $A(T) = A_1 / (1 + \exp(\frac{T-c_1}{c_2}))$, which provides an excellent empirical description of the data and allows us to determine $A(0)$. As the SO amplitude saturates at low temperatures, the exact extrapolation procedure has little effect on the value of $A(0)$ and the extrapolation is robust.

Finally, we use Eq. (2) to calculate $I_{\text{MR}}(T)$, which we plot in Fig. 4b. In Supplementary Fig. 5, we show $I_{\text{MR}}(T)$ for several different devices, showing consistency between the values extracted for any thickness, from ρ_{xx} or ρ_{yy} and from measurements along different crystallographic axes.

Ab initio calculations. The ab initio calculations were performed with the open source DFT code JDFTx⁴². We used fully relativistic Perdew–Burke–Ernzerhof pseudopotentials^{43–45} and included the spin-orbit coupling effect in all calculations. A kinetic energy cutoff of 28 Ha was used along with a $6 \times 6 \times 8\Gamma$ -centered *k*-mesh and a Fermi–Dirac smearing of 0.01 Ha for the Brillouin zone integration. Both the lattice constants and the ion positions were relaxed until the energy differences were less than 10^{-9} Ha. To compute the electron–phonon scattering time, we performed frozen phonon calculations in a $3 \times 3 \times 2$ supercell, and obtained 44 maximally localized Wannier functions by projecting the plane-wave bandstructure to *W* *d* and *P* *p* orbitals, which allowed us to converge the electron scattering calculation on a much finer $66 \times 66 \times 88\mathbf{k}'$ and \mathbf{q} grid for $T = 10 \text{ K}$.

Data availability

The data generated in this study have been deposited in the Zenodo repository, <https://doi.org/10.5281/zenodo.4675599>. Data presented in Fig. 4d, e are available upon request.

Received: 3 February 2021; Accepted: 21 July 2021;

Published online: 10 August 2021

References

- Zaenans, J. Electrons go with the flow in exotic material systems. *Science* **351**, 1026–1027 (2016).
- Levitov, L. & Falkovich, G. Electron viscosity, current vortices and negative nonlocal resistance in graphene. *Nat. Phys.* **12**, 672–676 (2016).
- Varnavides, G., Jermyn, A. S., Anikeeva, P., Felser, C. & Narang, P. Electron hydrodynamics in anisotropic materials. *Nat. Commun.* **11**, 4710 (2020).
- Sulpizio, J. A. et al. Visualizing Poiseuille flow of hydrodynamic electrons. *Nature* **576**, 75–79 (2019).
- Vool, U. et al. Imaging phonon-mediated hydrodynamic flow in WTe_2 with cryogenic quantum magnetometry. ArXiv 2009.04477 (2020).
- Gurzhi, R. N., Kalinenko, A. N. & Kopeliovich, A. I. Hydrodynamic effects in the electrical conductivity of impure metals. *Zh. Eksp. Teor. Fiz.* **96**, 1522–1532 (1989).
- Bufler, F. M. et al. Monte Carlo simulation and measurement of nanoscale n-MOSFETs. *IEEE Trans. Electron Devices* **50**, 418–424 (2003).
- Jazaeri, F., Beckers, A., Tajalli, A. & Sallese, J. M. A review on quantum computing: Qubits, cryogenic electronics and cryogenic MOSFET physics. ArXiv 1908.02656 (2019).
- Sondheimer, E. H. The influence of a transverse magnetic field on the conductivity of thin metallic films. *Phys. Rev.* **80**, 401–406 (1950).
- Gurevich, V. L. Oscillations in the conductivity of metallic films in magnetic field. *Sov. Phys. JETP* **35**(8), 464–470 (1959).
- Harrison, W. A. Electronic structure of polyvalent metals. *Phys. Rev.* **118**, 1190–1208 (1960).
- Hambourger, P. D. & Marcus, J. A. Size-dependent oscillatory magnetoresistance in cadmium. *Phys. Rev. B* **8**, 5567–5578 (1973).
- Rourke, P. M. & Julian, S. R. Numerical extraction of de Haas–van Alphen frequencies from calculated band energies. *Computer Phys. Commun.* **183**, 324–332 (2012).
- Mackey, H. J. & Sybert, J. R. Harmonic content of magnetomorph oscillations in the kinetic coefficients of electron transport due to partially specular boundary scattering. *Phys. Rev.* **158**, 658–661 (1967).
- Shoenberg, D. *Magnetic oscillations in metals* (Cambridge University Press, 1984).
- Autès, G., Gresch, D., Troyer, M., Soluyanov, A. A. & Yazzev, O. V. Robust Type-II Weyl Semimetal Phase in Transition Metal Diphosphides XP_2 ($X = \text{Mo}, \text{W}$). *Phys. Rev. Lett.* **117**, 066402 (2016).

17. Jaoui, A. et al. Departure from the Wiedemann-Franz law in WP_2 driven by mismatch in T-square resistivity prefactors. *npj Quantum Mater.* **3**, 64 (2018).
18. Gooth, J. et al. Thermal and electrical signatures of a hydrodynamic electron fluid in tungsten diphosphide. *Nat. Commun.* **9**, 4093 (2018).
19. Kumar, N. et al. Extremely high magnetoresistance and conductivity in the type-II Weyl semimetals WP_2 and MoP_2 . *Nat. Commun.* **8**, 1642 (2017).
20. Grishin, A., Lutsishin, P., Ostroukhov, Y. & Panchenko, O. Multiple Sondheimer oscillations in tungsten plates with atomically pure surfaces. *Sov. J. Exp. Theor. Phys.* **49**, 673 (1979).
21. Alstadheim, T. & Risnes, R. Sondheimer oscillations in aluminium single crystals. *Philos. Mag.* **18**, 885–894 (1968).
22. Kunzler, J. E. & Renton, C. A. “Size effect” in electrical resistivity measurements on single crystals of high-purity tin at liquid helium temperatures. *Phys. Rev.* **108**, 1397 (1957).
23. Babiskin, J. & Siebenmann, P. G. New type of oscillatory magnetoresistance in metals. *Phys. Rev.* **107**, 1249–1254 (1957).
24. Coulter, J. et al. Uncovering electron-phonon scattering and phonon dynamics in type-I Weyl semimetals. *Phys. Rev. B* **100**, 220301(R) (2019).
25. Narang, P., Garcia, C. A. & Felser, C. The topology of electronic band structures. *Nat. Mater.* **20**, 293–300 (2021).
26. Osterhoudt, G. B. et al. Evidence for dominant phonon-electron scattering in Weyl semimetal WP_2 . *Phys. Rev. X* **11**, 01107 (2021).
27. Moll, P. J. W. Focused ion beam microstructuring of quantum matter. *Annu. Rev. Condens. Matter Phys.* **9**, 147–162 (2018).
28. Shekhar, C. et al. Single crystal growth for topology and beyond. *Chemical Metals Science & Solid State Chemistry*. <https://www.cps.mpg.de/ssc/crystal-growth.pdf> (2018).
29. Kelley, R., Song, K., Van Leer, B., Wall, D. & Kwakman, L. Xe+ FIB milling and measurement of amorphous silicon damage. *Microsc. Microanalysis* **19**, 862–863 (2013).
30. Fuchs, K. The conductivity of thin metallic films according to the electron theory of metals. *Math. Proc. Camb. Philos. Soc.* **34**, 100–108 (1938).
31. Moll, P. J. W., Kushwaha, P., Nandi, N., Schmidt, B. & Mackenzie, A. P. Evidence for hydrodynamic electron flow in $PdCoO_2$. *Science* **351**, 1061–1064 (2016).
32. Schönemann, R. et al. Fermi surface of the Weyl type-II metallic candidate WP_2 . *Phys. Rev. B* **96**, 121108(R) (2017).
33. Bachmann, M. D. et al. Inducing superconductivity in Weyl semi-metal microstructures by selective ion sputtering. *Sci. Adv.* **3**, e1602983 288 (2017).
34. Van Delft, M. R. et al. Two- and three-dimensional superconducting phases in the Weyl semimetal TaP at ambient pressure. *Crystals* **10**, 288 (2020).
35. Kresse, G. & Furthmüller, J. Efficiency of ab-initio total energy calculations for metals and semiconductors using a plane-wave basis set. *Computational Mater. Sci.* **6**, 15–50 (1996).
36. Sato, H. Phonon-limited mean free path in the Sondheimer oscillation of aluminum. *J. Low. Temp. Phys.* **38**, 267–275 (1980).
37. Munarin, J. A., Marcus, J. A. & Bloomfield, P. E. Size-dependent oscillatory magnetoresistance effect in gallium. *Phys. Rev.* **172**, 718–736 (1968).
38. Liang, T. et al. Ultrahigh mobility and giant magnetoresistance in Cd_3As_2 : protection from backscattering in a Dirac semimetal. *Nat. Mater.* **14**, 280–284 (2015).
39. Gao, W. et al. Extremely large magnetoresistance in a topological semimetal candidate pyrite $PtBi_2$. *Phys. Rev. Lett.* **118**, 256601 (2017).
40. Zhang, C. L. et al. Electron scattering in tantalum monoarsenide. *Phys. Rev. B* **95**, 085202 (2017).
41. Ziman, J. M. *Electrons and phonons: the theory of transport phenomena in solids* (Oxford University Press, 2001).
42. Sundararaman, R. et al. JDFTx: Software for joint density-functional theory. *SoftwareX* **6**, 278–284 (2017).
43. Perdew, J. P., Burke, K. & Ernzerhof, M. Generalized gradient approximation made simple. *Phys. Rev. Lett.* **77**, 3865–3868 (1996).
44. Dal Corso, A. Pseudopotentials periodic table: From H to Pu. *Computational Mater. Sci.* **95**, 337–350 (2014).
45. Perdew, J. P. et al. Restoring the density-gradient expansion for exchange in solids and surfaces. *Phys. Rev. Lett.* **100**, 136406 (2008).
46. Coulter, J., Sundararaman, R. & Narang, P. Microscopic origins of hydrodynamic transport in the type-II Weyl semimetal WP_2 . *Phys. Rev. B* **98**, 115130 (2018).

Acknowledgements

M.R.v.D. acknowledges funding from the Rubicon research program with project number 019.191EN.010, which is financed by the Dutch Research Council (NWO). This project was funded by the European Research Council (ERC) under the European Union’s Horizon 2020 research and innovation program (grant no. 715730, MiTopMat). Y.W. is partially supported by the STC Center for Integrated Quantum Materials, NSF Grant No. DMR-1231319 for development of computational methods for topological materials. This research used resources of the National Energy Research Scientific Computing Center, a DOE Office of Science User Facility supported by the Office of Science of the U.S. Department of Energy under Contract No. DE-AC02-05CH11231 as well as resources at the Research Computing Group at Harvard University. P.N. is a Moore Inventor Fellow and gratefully acknowledges support through Grant No. GBMF8048 from the Gordon and Betty Moore Foundation. C.A.C.G. acknowledges support from the NSF Graduate Research Fellowship Program under Grant No. DGE-1745303. We acknowledge financial support from DFG through SFB 1143 (project-id 258499086) and the Würzburg-Dresden Cluster 274 of Excellence on Complexity and Topology in Quantum Matter - ct.qmat (EXC 2147, project-id 39085490). B.G. acknowledges financial support from the Swiss National Science Foundation (grant number CRSII5_189924). H.S. and B.G. thank J. Gooth for discussion and K. Moselund, S. Reidt, and A. Molinari for support, and received funding from the European Union’s Horizon 2020 research and innovation program under Grant Agreement ID 829044 “SCHINES”.

Author contributions

M.R.v.D., C.P., J.O., C.G., J.D. performed the transport experiments, as well as the microfabrication in collaboration with B.G. and H.S. The crystals were grown by V.S. and C.F., and crystallographically analyzed by H.B. Y.S. and C.F. calculated the band structures, and Y.W., G.V., C.A.C.G., P.N. performed the electron-phonon scattering calculations. B.G., C.F., P.N., and P.J.W.M. conceived the experiment, and all authors contributed to writing of the manuscript.

Competing interests

The authors declare no competing interests.

Additional information

Supplementary information The online version contains supplementary material available at <https://doi.org/10.1038/s41467-021-25037-0>.

Correspondence and requests for materials should be addressed to M.R.v.D., P.N. or P.J.W.M.

Peer review information *Nature Communications* thanks the anonymous reviewer(s) for their contribution to the peer review of this work. Peer reviewer reports are available.

Reprints and permission information is available at <http://www.nature.com/reprints>

Publisher’s note Springer Nature remains neutral with regard to jurisdictional claims in published maps and institutional affiliations.



Open Access This article is licensed under a Creative Commons Attribution 4.0 International License, which permits use, sharing, adaptation, distribution and reproduction in any medium or format, as long as you give appropriate credit to the original author(s) and the source, provide a link to the Creative Commons license, and indicate if changes were made. The images or other third party material in this article are included in the article’s Creative Commons license, unless indicated otherwise in a credit line to the material. If material is not included in the article’s Creative Commons license and your intended use is not permitted by statutory regulation or exceeds the permitted use, you will need to obtain permission directly from the copyright holder. To view a copy of this license, visit <http://creativecommons.org/licenses/by/4.0/>.

© The Author(s) 2021